JMEPEG (2009) 18:361–368
DOI: 10.1007/s11665-008-9297-2
©ASM International
1059-9495/$19.00

Effect of Microstructure and Environment on Static Crack Growth Resistance in Alloy 706

Ling Yang, Jeffrey A. Hawk, David J. Duquette, and Robin C. Schwant

(Submitted July 2, 2008)

The relationship between thermo-mechanical processing, resultant microstructure, and mechanical properties has been of interest in the field of metallurgy for centuries. In this work, the effect of heat treatment on microstructure and key mechanical properties important for turbine rotor design has been investigated. Specifically, the tensile yield strength and crack growth resistance for a nickel-iron based superalloy 706 has been examined. Through a systematic study, a correlation was found between the processing parameters and the microstructure. Specifically, differences in grain boundary and grain interior precipitates were identified and correlated with processing conditions. Further, a strong relationship between microstructure and mechanical properties was identified. The type and orientation of grain boundary precipitates affect time-dependent crack propagation resistance, and the size and volume fraction of grain interior precipitates were correlated with tensile yield strength. It was also found that there is a strong environmental effect on time-dependent crack propagation resistance, and the sensitivity to environmental damage is microstructure dependent. Microstructures with η decorated grain boundaries were more resistant to environmental damage through oxygen embrittlement than microstructures with no η phase on the grain boundaries. An effort was made to explore the mechanisms of improving the time-dependent crack propagation resistance through thermo-mechanical processing, and several mechanisms were identified in both the environment-dependent and the environment-independent category. These mechanisms were ranked based on their contributions to crack propagation resistance.

Keywords forging, heat treating, mechanical testing, non-ferrous metals, superalloys

1. Introduction

In traditional turbine rotor design, rotor life is limited by the low cycle fatigue capability of the material. In other words, design focus has been to avoid crack initiation as a result of thermal transients that propagate through the rotor during startup and shutdown. However, crack initiation is inevitable and results from several well-known mechanisms, including metallurgical defects, abusive machining, etc. Once a crack initiates, the life of the component is controlled by crack propagation. A growing crack can severely reduce the life of the turbine, and in the worst case, liberate part of the rotor. Thus, turbine rotors with damage tolerance against initial flaws below the detection limit of ultrasonic inspection methods are an important design requirement.

Other than in gas turbine rotor applications (Ref 1-3), alloy 706 has been considered as a candidate alloy for ultra supercritical (USC) steam turbine rotors for temperatures up to 700 °C (Ref 4-6). Under this severe operating condition, rotor lifting methodology by crack propagation must be considered, and the rotor alloy must have excellent crack propagation resistance. The objective of this study was to explore different alloy 706 microstructures developed *via* different thermo-mechanical processing routes and to evaluate the crack growth resistance of the different microstructures. The obvious benefit in doing this was to understand the relationship between certain aspects of the 706's microstructure and crack growth, which can lead to amelioration of catastrophic failure events. This would enable higher operating temperatures for turbines, with concomitant improvement in efficiency, leading to positive economic and environmental impacts.

Another important aspect of this work is to understand the role that environment has on alloy 706 mechanical behavior. Studies related to the effects of environment on the mechanical properties of superalloys can be traced back to the 1960s. In these studies, low cycle fatigue (LCF) testing at different frequencies in air and vacuum (Ref 7-9) were used to simulate rotor startup and shutdown. Results showed that the slower the frequency, the more intergranular the appearance of the fracture surfaces, and the lower the fatigue lifetime of the sample. In other words, LCF lifetime is not cycle dependent but time dependent. It was believed that the damaging species diffused along and embrittled the grain boundaries under the time-dependent loading condition, and thus caused life degradation, leading to intergranular failure (Ref 10). Oxygen was identified as the damaging species in air, and Andrieu et al. (Ref 11) showed that when the oxygen partial pressure was between 1.0 and 0.1 Pa, the crack propagation rate decreased by 3 orders of magnitude. At the high and the low end of the oxygen partial pressure range, crack growth rates were nearly constant.

Ling Yang, Jeffrey A. Hawk, and **Robin C. Schwant**, GE Energy, Schenectady, NY 12345; and **David J. Duquette**, Rensselaer Polytechnic Institute, Troy, NY 12180. Contact e-mail: lingyang@alum.rpi.edu.

In this study, three environments with various levels of oxygen partial pressure were used to better understand this effect on static crack propagation rate.

2. Procedure

2.1 Material

The samples used in this study were cut from a large size turbine forging. The forging was made from an ingot that was triple melt processed: The ingot was vacuum induction melted (VIM), followed by electro-slag re-melted (ESR), and finally vacuum arc re-melted (VAR). After VAR, the ingot was homogenized for an extended time to dissolve any Laves phases before it was billetized to break up the as-cast structure. Closed die forging was used to produce the final disc shape. Table 1 lists the chemical composition of this heat.

2.2 Heat Treatment

The as-received forging received the following heat treatment which was intended to maximize tensile properties: solution treated at 982 °C; fast cooled to room temperature; aged at 730 °C for 8 h; furnace cooled at 55 °C/h to 620 °C and held at 620 °C for 8 h; air cooled to room temperature. The as-received heat treatment is referred to as "A" in the following sections.

Half of the cut samples were re-heat treated per the following cycle: solution treated at 968 °C; furnace cooled to 816 °C and held at 816 °C for 5 h; fast cooled to room temperature; aged at 720 °C for 8 h; furnace cooled at 55 °C/h to 620 °C and held at 620 °C for 8 h; air cooled to room temperature. This additional heat treatment cycle is referred to as "B" in the following sections.

2.3 Microscopy

Scanning electron microscopy (SEM) and transmission electron microscopy (TEM) were used to evaluate the microstructures of alloy 706. SEM was also used for fracture surface examination.

Samples for TEM were sectioned into 1 mm slices using a diamond saw. These slices were mechanically ground to approximately 70 μm thickness using standard metallographic techniques. A core drill was used to extract a 3-mm-diameter disk. Final thinning of the foil was accomplished via electropolishing in a 20% perchloric acid/80% methanol solution at 100 °C, 20 V, and at 20 mA. A JEOL 2010 electron microscope, operating at 200 kV, was used to examine the specimens in bright and dark field imaging modes. Electron diffraction and energy dispersive X-ray spectroscopy (EDS) were also used to evaluate aspects of the microstructures.

2.4 Room Temperature Tensile Tests

Tensile tests at room temperature were performed in an Instron screw driven tensile test machine at Westmoreland Mechanical Testing & Research, Inc., Westmoreland, PA. The tensile test conditions conformed to ASTM E8. One difference in the test procedure is that a constant displacement rate of 0.005 mm/min was used until rupture to obtain smooth stress-strain curves. The yield strength was determined by the 0.2% offset technique as described in ASTM E8.

2.5 Static Crack Propagation Tests

Compact tension specimens were used in the static crack propagation tests. The thickness of the specimens is 6.35 mm with 0.635 mm deep side grooves as specified by ASTM E1457-92. The side-grooved specimens had an initial crack length of 4.0 mm and were subsequently fatigue pre-cracked at a frequency of 10-20 Hz at room temperature using an R ratio of 0.1 and a low stress intensity factor (ΔK). Sample pre-cracking was terminated when the overall crack length reached 5.3 mm. For these specimen dimensions, a stress concentration factor K of 30.8 MPa $\sqrt{\text{m}}$ is obtained at 4.89 MN.

The initial static crack growth tests were conducted in a creep stand in laboratory air. The specimen was first heated to the test temperature, i.e., 593 °C, and allowed to soak for several hours. After the temperature stabilized, the load was applied through the lever arm system of the creep stand. The temperature was controlled within ±3 °C using thermocouples, which were attached directly to the specimens.

The propagation rate of the fatigue pre-crack was not monitored during the initial 2-week (336 h) testing period. Instead, if the specimen fractured within the 2-week timeframe, the actual failure time was recorded. If the specimen did not fail, the static crack growth test was terminated at 336 h. The specimen was then broken and the length of the crack measured in order to determine the crack growth rate for this time interval.

3. Results

3.1 Microstructure

Grain size measurement of the "A" and "B" microstructures showed no difference, with an average grain diameter of 100-110 μm. However, SEM examinations, combined with TEM, revealed clear differences in the precipitation behavior between the two heat treatments.

3.1.1 Grain Boundary Precipitates. Straight grain boundaries were most prevalent in "A". As shown in Fig. 1 and 2, these grain boundaries are relatively free of precipitates except for blocky carbides, i.e. (Nb, Ti)C. The grain boundary profiles are straight.

Grain boundaries with cellular η precipitates that lie parallel to each other are prevalent in microstructure "B". The length of the η plates ranges from one to several microns (see Fig. 3 and 4). The η precipitates are rich in Ni and Ti. It has been documented that η has a specific orientation relationship with the γ matrix: $\{0001\}\eta//\{111\}\gamma$ and $\langle 1210\rangle\eta//\langle 110\rangle\gamma$ (Ref 12, 13).

Table 1 Chemical composition of alloy 706 (wt.%, balance Fe)

Ni	Cr	Nb + Ta	Ti	Al	C	Cu	Mn	Si	S	P	B	Co
41.3	16.0	3.03	1.6	0.245	0.018	0.013	0.037	0.069	0.0005	0.0056	0.0014	0.023

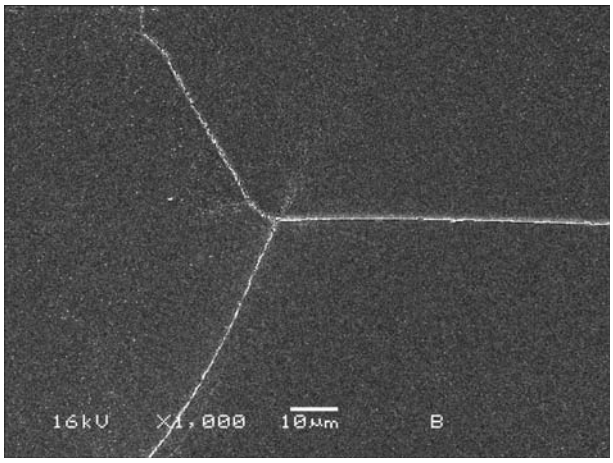

Fig. 1 Straight grain boundary in microstructure "A" as shown by SEM

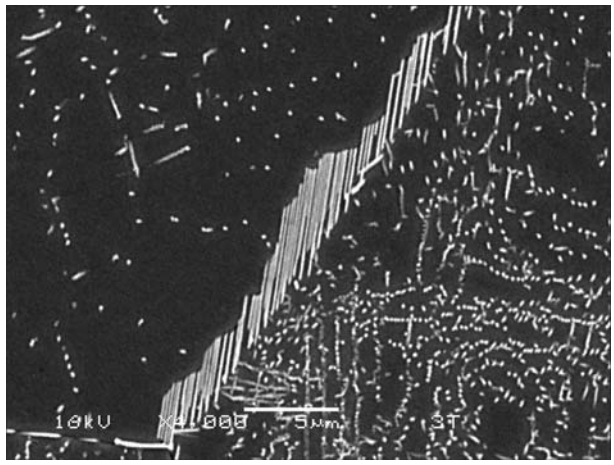

Fig. 3 SEM micrograph of a grain boundary in microstructure "B" showing cellular η precipitates

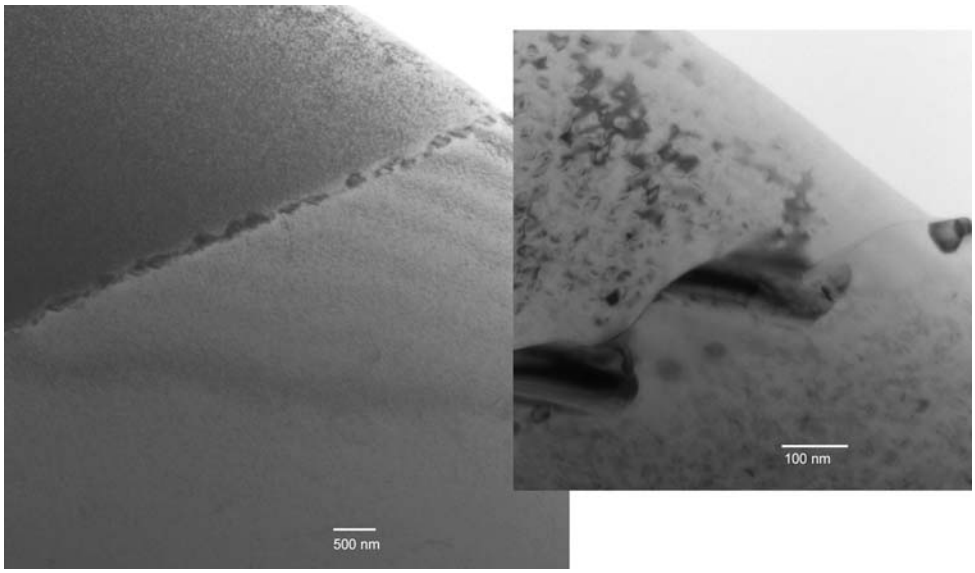

Fig. 2 Straight grain boundary in microstructure "A" as shown by TEM

Thus, the η phases are parallel to each other in order to meet this orientation relationship. Figure 5 is an example of a case where the η platelets grow from a grain boundary into a single grain in two different orientations.

Figure 6 shows two bright field images tilted to reveal contrast differences between adjacent grains. Based on the contrast difference, it was observed that this group of η precipitates belongs to the left-hand side grain in these micrographs. The η precipitates nucleate on the straight grain boundary and grow into one of the adjacent grains depending on which grain has the most favorable orientation. The resulting η growth defines a new grain boundary profile and follows the tips of the η precipitates. This new grain boundary is more tortuous and appears serrated optically or in the SEM at low magnification. This is typical cellular precipitation behavior (Ref 14, 15). Another observation seen in Fig. 4 and 6 is that the new grain boundary profile occurs at the tips of the η precipitates, and this region is characterized by a continuous precipitate free zone (PFZ).

The η consists primarily of Ni and Ti with the Ni and Ti diffusing to the tips of η during growth. Thus, the microchemistry of the PFZ will vary from that of the matrix. Table 2 shows the EDS results of the PFZ local chemistry measurements at the grain boundary and from selected matrix locations of similar thickness to the PFZ measurement point.

Comparing the matrix and PFZ chemistries, the PFZ is lean in Ti and Ni, and rich in Cr and Fe. Further EDS analysis was conducted at several other locations: (1) along the centerline of two η precipitates and (2) adjacent to the η precipitate. The measurements were compared with other measurements within the grain boundary PFZ. It was found that PFZ chemistry is uniform and independent of location.

The higher Cr level in the PFZ can be explained in the following way. Solubility of Cr in the η phase is low. During the precipitation of grain boundary η, Ti and Ni are consumed from the matrix region adjacent to the growing plate. Thus, Ti and Ni, which are usually available to form γ'/γ'' within the matrix, were not available where η precipitated. As a result, a

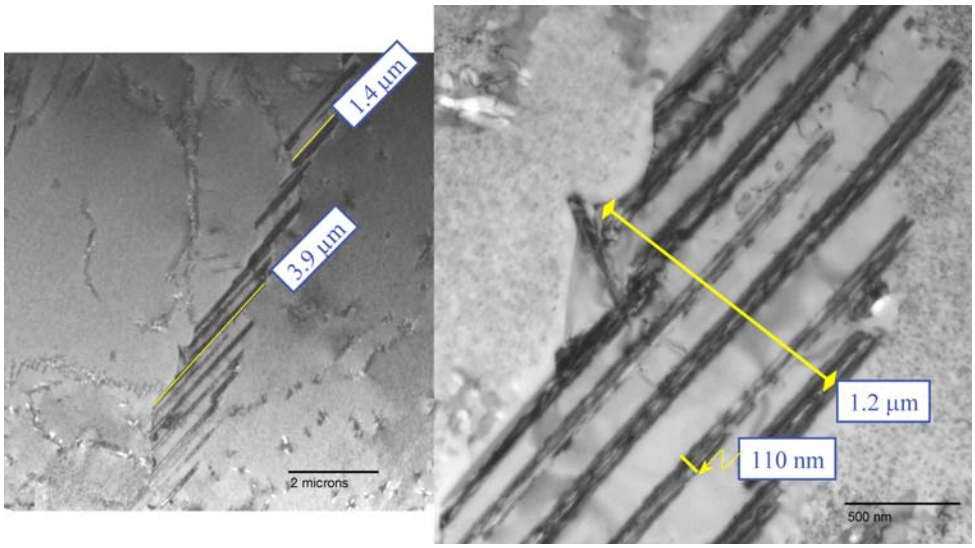

Fig. 4 TEM micrograph of a grain boundary in microstructure "B" showing cellular η precipitates

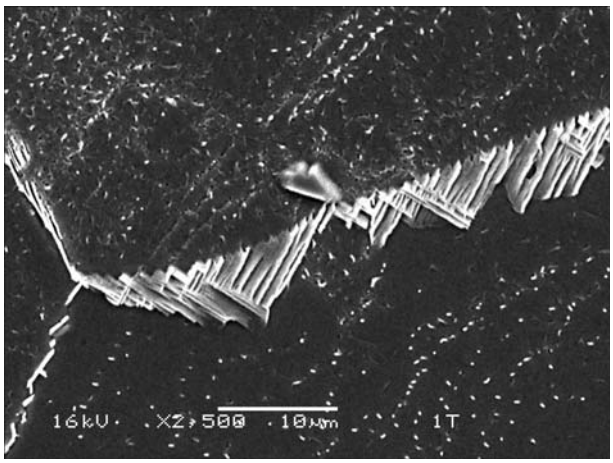

Fig. 5 SEM micrograph of a grain boundary in microstructure "B" showing cellular η precipitates growing from a grain boundary into a single grain at two orientations

PFZ formed which was rich in Cr. Similar values at various locations between η plates are due to the rapid diffusion of Ni and Ti during the cellular precipitation of the η phase, combined with the fine spacing of η precipitates in microstructure "B".

3.1.2 Grain Interior Precipitates. Figure 7 shows a uniform distribution of γ′/γ″ precipitates in microstructure "A", which are approximately 20 nm in diameter. High magnification dark field imaging showed γ′/γ″ co-precipitates with a non-compact structure. This is consistent with other alloy 706 literature (Ref 16-18). This type of γ′/γ″ co-precipitation has also been reported in alloy 718 (Ref 19-22).

The bright-field image of microstructure "B" on the left in Fig. 8, and the dark-field image taken from the fine precipitate region to the right, showed many lenticular-type precipitates. These precipitates are more than 100 nm in length and coexist with fine and uniform γ′/γ″ precipitates similar to those observed in microstructure "A".

The lenticular-type precipitates grow in certain orientations relative to the matrix. Based on selected area diffraction (SAD),

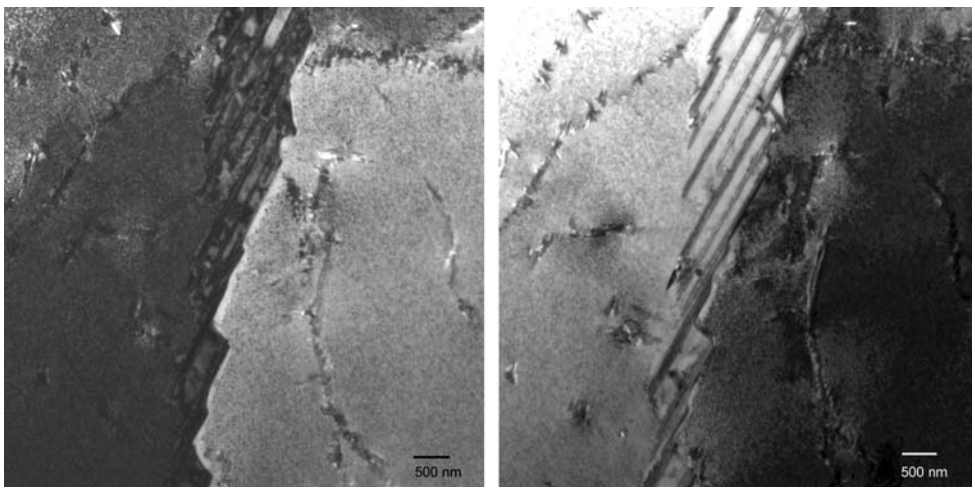

Fig. 6 TEM micrograph of a grain boundary in microstructure "B" showing cellular η precipitates and the serrated nature of the grain boundary

Table 2 The PFZ and the matrix chemistry of a serrated grain boundary in microstructure "B"

Element	Weight %	Atomic %	Uncertainty %	Correction	*K*-factor
PFZ					
Ti(K)	0.364	0.429	0.06	0.985	1.299
Cr(K)	18.617	20.222	0.354	0.991	1.376
Fe(K)	41.041	41.506	0.551	0.994	1.48
Ni(K)	38.216	36.771	0.552	0.996	1.592
Nb(K)	1.759	1.069	0.186	0.999	4.209
Matrix					
Ti(K)	1.078	1.278	0.085	0.985	1.299
Cr(K)	15.165	16.568	0.311	0.991	1.376
Fe(K)	37.616	38.262	0.503	0.994	1.48
Ni(K)	44.002	42.582	0.564	0.996	1.592
Nb(L)	2.136	1.306	0.153	0.894	2.837

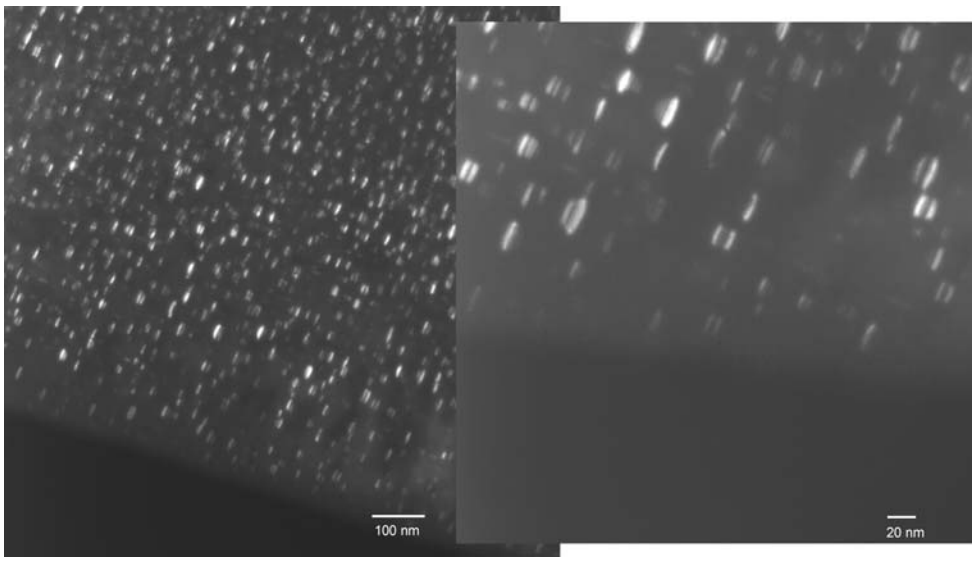

Fig. 7 TEM micrographs of the grain interior precipitates in microstructure "A"

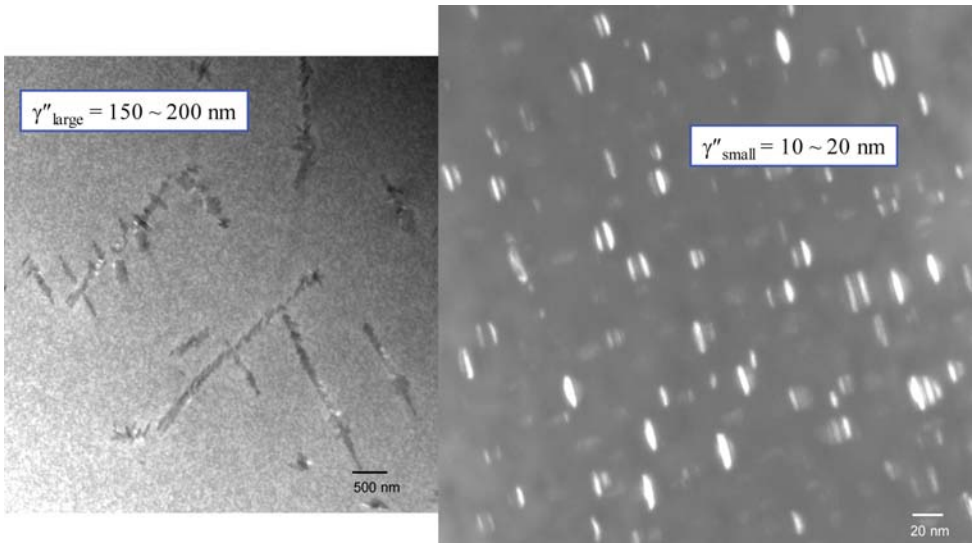

Fig. 8 TEM micrographs of the grain interior precipitates in microstructure "B"

they were identified as BCT γ″. The coarsened γ″ has been found in alloy 718, usually after an extended aging treatment (Ref 19, 22). These coarsened γ″ phases appear to follow certain patterns, and the fine γ′/γ″ co-precipitates in "B" are of the same size as in "A".

3.2 Mechanical Behavior

The results of room temperature tensile tests and static crack growth tests at 593 °C are summarized in Table 3. After using heat treatment "B", room temperature 0.2% yield strength and ultimate tensile strength (UTS) were reduced by 7 and 4%, respectively. In contrast, the static crack propagation resistance, as measured by time to failure during static loading, was significantly improved. That is, the specimen did not fail in the 2-week time period of the test, and fracture surface examination showed minimal crack growth. Specimen "A" fractured in a very short period of time.

4. Discussion

4.1 Correlations Between Heat Treatment, Microstructure, and Mechanical Properties

Microstructure "A" experienced fast cooling after solution treatment and after subsequent aging at low temperature. This heat treatment resulted in a fine and uniform distribution of γ′/γ″ co-precipitates and straight, featureless grain boundaries. Microstructure "B", on the other hand, experienced slow cooling after solution treatment and an intermediate hold at 816 °C, which is well within the η precipitation range. During the hold at 816 °C, cellular η precipitated and the grain boundaries migrated.

Since the hold at 816 °C is close to the minimum time at temperature for γ′/γ″ precipitation (Ref 23), γ″ also precipitated and coarsened during this portion of the heat treatment. Subsequently, fine and uniform γ′/γ″ precipitated in the matrix as a result of the two-step aging sequence, and as a result, microstructure "B" possessed a bimodal distribution of γ″ precipitates in the grain interior, and serrated grain boundaries with η precipitates along the boundary.

Since γ″ is the primary strengthening phase in alloy 706 (Ref 24), and because γ″ exhibits a high coherency strain with the matrix (Ref 12), the strengthening effect of γ″ can be significantly reduced by particle coarsening. This explains why heat treatment "B" with a bimodal distribution of γ″ had lower yield strength than heat treatment "A". The grain boundary η precipitation may also contribute to the yield strength reduction because its formation consumes Ti, which contributes to alloy strength through the formation of γ′/γ″ precipitates in the matrix.

To understand the improvement in static crack propagation resistance that heat treatment "B" imparts, the fractographic characteristics of the static crack growth region were examined. As mentioned in the experimental section, the compact tension specimen from heat treatment "B" was broken apart and the slow crack growth fracture surfaces were compared with those of heat treatment "A", that is, the sample that had completely failed after 8 h in the static crack growth test.

A narrow intergranular region was detected on the fracture surfaces of heat treatment "B", which confirmed that the crack grew during the 2-week static loading period. For comparison as shown in Fig. 9, the grain boundaries in heat treatment "A" are intergranular, featureless, and smooth (see also Fig. 1 and 2). The appearance of these grain boundaries suggests a brittle failure mode with a low cohesive energy. Heat treatment "B" also results in a much rougher surface with η on the grain boundaries (see Fig. 3 and 4). The differences in grain boundary precipitate morphology and grain boundary shape clearly affect static crack growth resistance. Samples of microstructure "A" with dissociated small precipitates in a virtually flat boundary exhibit rapid static crack growth rates while samples from heat treatment "B" with large, discontinuous η precipitates in a heavily serrated boundary exhibit very slow static crack propagation rates.

Table 3 Summary of mechanical testing results

	HT "A"	HT "B"
RT tensile		
0.2% YS, MPa	1060	989
UTS, MPa	1249	1196
593 °C crack growth		
Time to failure, h	8	>336

4.2 Environmental Effect

Earlier work on alloy 718 (Ref 25) credited the slower crack growth rate of overaged alloy 718 to more rapid stress relaxation as a result of its lower yield strength, compared to conventionally aged 718. In other words, that work only recognized the bulk properties of the alloy, ignoring either local microstructural effects such as grain boundary structure or

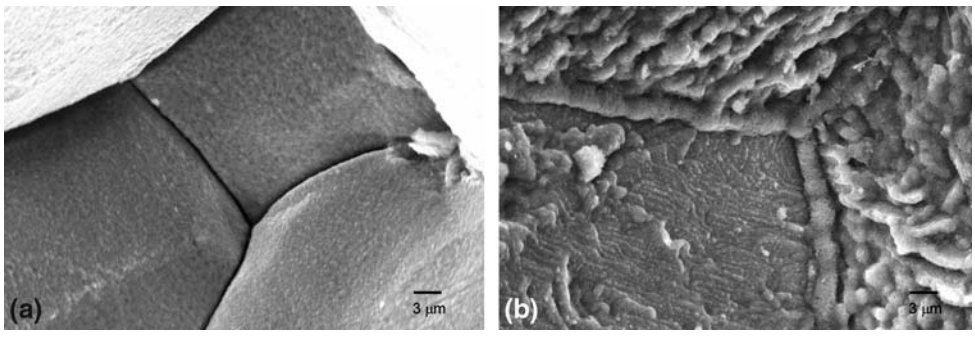

Fig. 9 SEM fractography of intergranular crack growth region: (a) heat treatment "A" and (b) heat treatment "B"

Table 4 Summary of environmental effects on static crack growth rate

ID	Environment	O_2 partial pressure, Pa	TTF, h
1	Air	2.8×10^4	8
2	Argon	19	31.5
3	Vacuum	1.9×10^{-4}	No growth

environmental effects. Therefore, in order to differentiate between creep crack growth and any environmental effects for alloy 706, two additional static crack growth tests were performed on specimens from heat treatment "A" under identical loading conditions but with different environments.

One test was conducted in 99.9% pure argon. During this test, argon flow in the test chamber was maintained at a positive pressure of 6.89×10^4 Pa. The specimen fractured after 31.5 h of exposure at load. Based on the monitored pressure during testing, and the purity of argon, the oxygen partial pressure was calculated as 19 Pa. This pressure is higher than the transition pressure: 0.1-1.0 Pa reported in Ref 11 for alloy 708.

Another test was performed in a vacuum chamber at the Mechanical Engineering Department at the University of Tennessee. A 6.67×10^{-4} Pa vacuum was maintained throughout the test. The specimen did not fracture during the 2-week period, and crack opening displacement (COD) measurement, and metallographic examination of the specimen, showed no crack growth. A summary of the three environmental tests is shown in Table 4.

The significant difference in time to failure clearly indicates a strong oxygen partial pressure dependence on static crack propagation rate, i.e., crack grows very fast at high oxygen partial pressure with low growth rates at a partial pressure approximately three orders of magnitude less than that of air and no growth whatsoever at low oxygen partial pressures. These comparison tests have shown that heat treatment "B" caused alloy 706 to be less prone to oxygen embrittlement in air. It may be surmised that, in the absence of oxygen, no crack growth would have occurred for samples exhibiting the "B" microstructure.

The factors differentiating the static crack growth resistance of alloy 706 of heat treatments "A" and "B" in air can be summarized as follows:

- Grain boundary local chemistry modification. Cellular precipitation of η causes a precipitate free zone and local chemistry changes along newly formed grain boundaries. The PFZ is enriched in Cr, which improves the oxidation resistance of the near grain boundary region. A similar beneficial effect of Cr on environmental crack growth resistance has also been observed for other high-temperature alloys (Ref 11, 26-31). There is, however, at least one report of an improvement in static crack growth for alloy X-750, where the formation of $M_{23}C_6$ resulted in lean Cr from the PFZ. In that case the improvement in static crack growth appeared to be linked to the tortuous crack path created by the carbide precipitation (Ref 32). Thus, resistance to static crack growth is a function of both the environmental resistance of the crack path as well as the morphology of the crack path.
- Under most scenarios, the PFZ should be the weakest mechanical link in the alloy since it is essentially a solid solution alloy, which is in contrast to the precipitation hardened matrix. However, the enhanced oxidation resistance of the PFZ effectively promotes a Cr oxide layer at the crack tip, which inhibits further environmental access to the grain boundary area.
- It is also possible that incoherent η phase boundaries trap oxygen atoms. A similar mechanism has been postulated for alloy 718 (Ref 33). Because η is coherent with the grain where the original grain boundary is located, and incoherent with the newly migrated grain boundary, the incoherent interface has the ability to trap oxygen atoms. Thus, heat treatment "B" enhances the ability of the grain boundary to trap oxygen atoms, thus slowing down the oxygen diffusion to the crack tip.
- The serrated grain boundaries also reduce the local stress concentration factor and the increased ductility of the PFZ can possibly blunt the growing cracks, which can also contribute to the improvement in crack propagation resistance. However, the most dominant factor seems to be the oxygen partial pressure.

5. Conclusion

Through microstructure and mechanical property evaluation on alloy 706 using two different heat treatments, the following conclusions can be drawn:

1. Static crack growth resistance of heat treatment "A" is strongly dependent on environment. Oxygen in air caused grain boundary embrittlement and accelerated the crack growth along grain boundaries.
2. Heat treatment "B" significantly reduced alloy 706's sensitivity to grain boundary embrittlement in air. The improvement is a function of the modification of the grain boundary morphology and local chemistry through cellular η precipitation, and not through a change in the bulk mechanical properties.

Acknowledgments

Management support from Dr. Jonathan Schaeffer at GE Energy is gratefully acknowledged and appreciated. The authors would also like to extend their sincere appreciation to Mr. Mike Larsen for the TEM examination, and Dr. Laurent Cretegny and Mr. Brian Cerniglia for the static crack growth testing in air and argon at GE Global Research Center. Thanks to Professor Peter Liaw at University of Tennessee for performing the static crack growth testing in vacuum.

References

1. P.W. Schilke and R.C. Schwant, Alloy 706 Use, Process Optimization, and Future Directions for GE Gas Turbine Rotor Materials, *Superalloys 718, 625, 706 and Various Derivatives,* 2001, p 25–34
2. P.W. Schilke, J. Pepe, and R.C. Schwant, Alloy 706 Metallurgy and Turbine Wheel Application, *Superalloys 718, 625, 706 and Various Derivatives*, 1994, p 1–12

3. S.V. Thamboo, L. Yang, and R.C. Schwant, Large Forgings of Alloy 706 and Alloy 718 for Land Based Gas Turbines, *14th International Forgemasters Meeting Weisbaden*, September 2000, p 330–335
4. S. Schubert, H.J. Penkalla, and J. Rösler, Wrought Ni-Base Alloys for Rotor Shafts in Advanced USC Power Plants, *Proceedings from the Fourth International Conference on Advances in Materials Technology for Fossil Power Plants*, Hilton Head Island, South Carolina, October 2004, p 587–601
5. C. Berger, J. Granacher, and A. Thoma, Creep Rupture Behaviour of Nickel Base Alloys for 700°C – Steam Turbines, *Superalloys 718, 625, 706 and Various Derivatives*, 2001, p 489–499
6. H.J. Penkalla, J. Wosik, W. Fischer, and F. Schubert, Structural Investigation of Candidate Materials for Turbine Disc Applications Beyond 700°C, *Superalloys 718, 625, 706 and Various Derivatives*, 2001, p 279–290
7. L.F. Coffin Jr., The Effect of High Vacuum on the Low-Cycle Fatigue Law, *Metall. Trans.*, 1972, **3**(7), p 1777–1788
8. R.H. Cook and R.P. Skelton, Environment-Dependence of the Mechanical Properties of Metals at High Temperature, *Int. Metall. Rev.*, 1974, **19**, p 199–222
9. D.A. Woodford, H.D. Solomon, and L.F. Coffin, The Effect of Temperature and Environment on Low Cycle Fatigue of Two Superalloys, *Proceedings of the Second International Conference on Mechanical Behavior of Materials*, 1976, p 893–897
10. D.A. Woodford, Gas Phase Embitterment and Time Dependent Cracking of Nickel Based Superalloys, *Energy Mater.*, 2006, **1**(1), p 59–79
11. E. Andrieu, G. Hochstetter, R. Molins, and A. Pineau, Oxidation Mechanisms in Relation to High Temperature Fatigue Crack Growth Properties of Alloy 718, *Superalloys 718, 625, 706 and Various Derivatives*, 1994, p 619–631
12. E.E. Brown and D.R. Muzyka, Nickel-Iron Alloys, *Superalloys II—High Temperature Materials for Aerospace and Industrial Power*, Wiley-Interscience, John Wiley and Sons, 1987, p 165–188
13. L. Remy, J. Laniesse, and H. Aubert, Precipitation Behavior and Creep Rupture of 706 Type Alloys, *Mater. Sci. Eng.*, 1979, **38**, p 227–239
14. D.A. Porter and K.E. Easterling, Diffusional Transformations in Solids, *Phase Transformations in Metals and Alloys*, 2nd edn. CRC Press, Reprinted in 2000 by Stanley Thornes Ltd., 1992, p 263–381
15. M.J. Donachie and S.J. Donachie, Structure/Property Relationships, *Superalloys – A Technical Guide*, 2nd edn. ASM International, p 211–286
16. T. Shibata, T. Takahashi, Y. Shudo, M. Kusuhashi, J. Taira, and T. Ishiguro, Effect of Cooling Rate From Solution Treatment on Precipitation Behavior and Mechanical Properties of Alloy 706, *Superalloys 718, 625, 706 and Various Derivatives*, 1997, p 379–388
17. T. Shibata, Y. Shudo, T. Takahashi, Y. Yoshino, and T. Ishiguro, Effect of Stabilizing Treatment on Precipitation Behavior of Alloy 706, *Superalloys 1996*, R.D. Kissinger et al., Eds., TMS, Warrendale, PA, 1996, p 627–636
18. T. Takahashi, T. Shibata, J. Taira, and T. Kure, Compositional Modification of Alloy 706, *Superalloys 718, 625 and Various Derivatives*, 2001, p 269–278
19. D.F. Paulonis, J.M. Oblak, and D.S. Duvall, Precipitation in Nickel Base Alloy 718, *Trans. ASM*, 1969, **62**, p 611–622
20. R. Cozar and A. Pineau, Morphology of γ' and γ'' Precipitates and Thermal Stability of Inconel 718 Type Alloys, *Metall. Trans.*, 1973, **4**, p 47–59
21. M.G. Burke and M.K. Miller, Precipitation in Alloy 718: A Combined AEM and APFIM Investigation, *Superalloys 718, 625, 706 and Various Derivatives*, 1991, p 337–350
22. J.P. Collier, S.H. Wong, J.C. Phillips, and J.K. Tien, The Effect of Varying Al, Ti and Nb Content on the Phase Stability of Inconel 718, *Metall. Trans. A*, 1988, **19**, p 1657–1666
23. K.A. Heck, The Time-Temperature-Transformation Behavior of Alloy 706, *International Special Emphasis Symposium on Superalloys 718, 625, 706 and Derivatives*, 1994, p 393–404
24. E.L. Raymond and D.A. Wells, Effects of Aluminum Content and Heat Treatment on Gamma Prime Structure and Yield Strength of Inconel Nickel-Chromium Alloy 706, *Superalloys – Processing*, Metals and Ceramics Information Center, Columbus, OH, 1972, p N1–N21
25. R. Molins, J. Chassaigne, and E. Andrieu, Oxidation Assisted Crack Propagation of Alloy 718, *Superalloys 718, 625, 706 and Various Derivatives*, 1997, p 655–664
26. J.S. Smith and K.A. Heck, Development of A Low Thermal Expansion, Crack Growth Resistant Superalloy, *Superalloys*, TMS, 1996, p 91–100
27. K.-M. Chang, Metallurgical Control of Fatigue Crack Propagation in Alloy 718, *Superalloys 718, 625 and Various Derivatives*, 1991, p 447–456
28. P.F. Browning, Time Dependent Crack Tip Phenomena in Gas Turbine Disk Alloys, Ph.D. Thesis, Rensselaer Polytechnic Institute, Troy, NY, 1998
29. E. Andrieu, G. Hochstetter, R. Molins, and A. Pineau, Oxidation and Intergranular Cracking Behavior of Two High Strength Ni-Base Superalloys, *Corrosion-Deformation Interactions*, Fontainebleu, France, October 5–7, 1992, p 479–491
30. R.H. Bricknell and D.A. Woodford, Grain Boundary Embrittlement of the Iron-base Superalloy IN903A, *Metall. Trans. A*, 1981, **12**, p 1673–1680
31. D.A. Woodford and R.H. Bricknell, Environmental Embrittlement of High Temperature Alloys by Oxygen, *Mater. Sci. Technol.*, 1983, **25**, p 157–199
32. S. Floreen, Microstructural and Environmental Effects During Creep Crack Growth in a Superalloy, *Elastic-Plastic Fracture: Second Symposium, Volume I – Inelastic Crack Analysis, ASTM STP 803*, C.F. Shih and J.P. Gudas, Eds., American Society for Testing and Analysis, 1983, p I-708– I-720
33. S.D. Antolovich, The Effect of Metallurgical Instabilities on The Behavior of IN718, *Superalloys 718—Metallurgy and Applications*, 1989, p 647–653